Published by
NIGERIAN SOCIETY OF PHYSICAL SCIENCES
Available online @ https://journal.nsps.org.ng/index.php/jnsps

J. Nig. Soc. Phys. Sci. 4 (2022) 909

Journal of the Nigerian Society of Physical Sciences

Synergistic Study of Reduced Graphene Oxide as Interfacial Buffer Layer in HTL-free Perovskite Solar Cells with Carbon Electrode

Sherifdeen O. Bolarinwa[a], Eli Danladi[b,*], Andrew Ichoja[b], Muhammad Y. Onimisi[a], Christopher U. Achem[c]

[a]*Department of Physics, Nigerian Defence Academy, Kaduna, Nigeria*
[b]*Department of Physics, Federal University of Health Sciences, Otukpo, Benue State, Nigeria*
[c]*Centre for Satellite Technology Development-NASRDA, Abuja, Nigeria*

Abstract

Perovskite Solar Cells (PSCs) being the most advanced photovoltaic technology today have attracted global attention due to its solution processability and cost effectiveness. In this paper, we reported the performance of perovskite solar cells by integrating Reduced Graphene Oxide (rGO) as a buffer layer. The combined effect of Ultraviolet visible (UV-vis) spectroscopy, X-ray Diffractometer (XRD), Raman spectroscopy, Scanning Electron Microscopy (SEM), Four Point Probe and Solar Simulator were used to explore the absorbance, crystallinity, morphological, resistivity and current voltage behavior of the photoanodes and devices. The rGO was deposited on top the mesoporous Titanium dioxide (m-TiO_2) (Device B), on methylammonium lead triiodide ($CH_3NH_3PbI_3$) perovskite absorber (Device C) and on m-TiO_2 & $CH_3NH_3PbI_3$ perovskite absorber (Device D). The reference device (Device A) was fabricated without rGO as a bench mark for comparison. From the results obtained, the devices with rGO show significant improvement over the device lacking rGO. The reference device gave a Short Circuit Current Density (Jsc) of 8.151 mAcm^{-2}, Open Circuit Voltage (Voc) of 0.575 V, Fill Factor (FF) of 74.4 % and Power Conversion Efficiency (PCE) of 3.49 %. The best performing device was the one with rGO incorporated on both m-TiO_2 and $CH_3NH_3PbI_3$. The device gave a Jsc of 8.737 mAcm^{-2}, Voc of 0.836 V, FF of 68.1% and PCE of 4.98 %. The device experienced an enhancement of ~ 7.20 % and 42.69 % in Jsc and PCE over the pristine device. This investigation aids the fundamental understanding of the effect of Graphene Materials (GRMs) on the optoelectronic properties of PSCs, and it further confirms the promising prospects of achieving low-cost, efficient and stable PSCs for commercialization with graphene materials.

DOI:10.46481/jnsps.2022.909

Keywords: Perovskite solar cells, Reduced Graphene Oxide, Buffer layer, HTM

Article History :
Received: 01 July 2022
Received in revised form: 02 August 2022
Accepted for publication: 04 August 2022
Published: 17 August 2022

Communicated by: Edward Anand Emile

1. Introduction

Perovskite Solar Cells (PSCs) in the history of Photovoltaic Technology (PVT) has witnessed a meteoric rise to prominence in terms of efficiency. From 3.8 % as demonstrated by Kojima and colleagues to a certified efficiency of 25.5 % [1]. This

*Corresponding author tel. no: +2348063307256
Email address: danladielibako@gmail.com (Eli Danladi)

powerful success can be attributed to the high carrier mobility, robust broadband absorption, long diffusion length, solution processability, design flexibility and low-cost of the metal halide perovskite [2-7]. The halide absorber is a crucial layer in PSC, that is responsible for absorbing light, creating photostimulated carriers, and transfers the carriers into the PSC network for electrical generation. The perovskite absorber is featured by AMX_3 crystal pattern, where the first letter A represents organic cation, the second letter M represents metal and the third letter X represents halogen atom. The architectural flexibility that allows for creativity has contributed to the wide acceptability and attention that PSCs are witnessing [1]. One of such architectures that has gained research attention is the Hole Transport Layer (HTL) free PSCs.

In 2013, Han's group reported for the first time in literature, a Hole Transport Material (HTM)-free mesoscopic PSCs with carbon electrode as replacement to Spiro-OMeTAD with PCE of 6.64 % [8, 9]. This architecture has been widely studied with several modifications owing to their relatively low production cost and low hysteresis [2, 10]. In addition, mesoscopic HTL-free PSCs are characterized by their long-term stability and therefore makes them a more suitable and promising architecture for commercialization [2, 6, 11-13]. However, optimization of solar device components remains an efficient way of enhancing overall device performance [1, 2, 8].

Despite these attained heights, PSCs are still hindered by several challenges such as poor stability under ambient conditions like humidity, heat, oxygen and UV light [1, 14-16], and couple with disparity in forward and reverse scan of Current-Voltage (I-V) characteristics [10]. These challenges sum up the basic reason why PSCs are yet to get to rooftop despite attaining the rivalry efficiency of current market PVT. Hence, the fabrication of efficient PSCs requires the crystallinity and morphology optimization of the perovskite films. Investigations has shown that grain sizes, film homogeneity plays critical roles in the optoelectronic quality of the film [17, 18]. In other words, controlling nucleation process is an efficient way of improving the properties of the perovskite absorbing material and in turn the device performance [17]. Apparently, thick layers with large and uniform grains of perovskite nanocrystals as absorbers enhances solar conversion efficiency. For a HTL-free PSC, the absorbing material gets sandwiched between the commonly employed Titania (TiO_2) as Electron Transport Layer (ETL) and the back contact [10].

The integration of carbon-based materials has been proposed and successfully integrated into PSCs to address the aforementioned drawbacks at the perovskite interface [2, 19-22]. Amongst these materials, the graphene, a 2-dimesnional material with zero bandgap appears to stand out owing to its low resistivity, efficient ambipolar charge transport, optical transparency, high thermal conductivity, mechanical strength, and flexibility [2, 20]. Its hydrophobic nature is an advantage that is capable of arresting instability of the perovskite film due to ambient conditions [2].

Because of its high electrical properties and presence of oxygenated moieties which makes it dispersible in polar solvents, rGO has been favored amidst other graphene materials. These factors result in high functionality of both the $CH_3NH_3PbI_3$ absorbing layer and the ETL.

A handful of literatures have reported the integration of rGO as a buffer layer between the charge carrier transport layer and perovskite layer [2, 23-25], however, the role of rGO is yet to be clearly elucidated. Herein, we reported a synergistic approach towards determining the actual role of rGO in perovskite solar cells. Rather than focus on obtaining high efficiency, this investigation sets to determine the most significant interface for the incorporation of rGO in HTL-free mesoporous PSCs. The commonly two step sequential deposition in air protocol was utilized while the graphene oxide was thermally reduced. Our approach has birthed a fundamental understanding on the utilization of rGO as buffer layer in perovskite interface.

2. Materials and Methods

2.1. Preparation of Reduced Graphene Oxide

In principle, obtaining reduced graphene oxide from graphite powder involves three fundamental stages namely; oxidation, exfoliation and reduction. The preparation of rGO in this investigation follows from the famous Tours method [26-28] with some fundamental precooling and reordering of the protocols. First, we obtained graphite ore from the Raw Materials Research and Development Council (RMRDC), Abuja, Nigeria. The graphite ore was then mashed into powdery form. A refrigerated mixture of 180 ml of concentrated sulfuric acid (H_2SO_4) and 20 ml of phosphoric acid (H_3PO_4) at 15 ^oC was gradually emptied into a beaker containing 1.5 g of untreated graphite powder. The resulting mixture was then placed in a 35 ^oC water bath. While stirring on a magnetic stirrer, 9 g of potassium permanganate ($KMnO_4$) was slowly added. A rise in temperature was observed with the addition of $KMnO_4$. The mixture was left to stir continually till its temperature drops to room temperature. This process lasted for 12 hours after which a graphite oxide was obtained. Next, is the dispersion of the as-obtained graphite oxide into 200 ml of distilled water to end the reaction. This was then gradually heated to 50 ^oC for 12 hours using a temperature-controlled water bath on a magnetic stirrer. As this process extended, the mixture thickened into a black paste. 1.5 ml of hydrogen peroxide (H_2O_2) was added to the obtained black paste and allowed to stir for 1 hour. Bubble was observed with a bright brown coloration, thus, indicating high level of oxidation. Next was filtration using a filter paper and collection of the GO then followed by rinsing of the GO with 200 ml Aqueous hydrochloric acid (HCl), distilled water and methanol each. The rinsing protocol was repeated thrice. The rinsed mixture was aliquoted, and some were thermally reduced. The gradual thermal reduction was first achieved at 120 ^oC for 5 minutes and then at 200 ^oC for 10 minutes and finally, 300 ^oC for 10 minutes to allow adequate reduction. Unlike reported journals where the starting graphite powder is mostly pretreated, this investigation reports the successful synthesis of graphene materials from untreated graphite ore.

2.2. Preparation of Precursors

2.2.1. Electron Transporting Material

Compact and Mesoporous TiO_2 were employed as the ETL. For the compact layer, the precursor was prepared using titanium isopropoxide, acetyl acetone and propanol as detailed in the well-established method of Wojciechowski et al. [29], while for the mesoporous layer, the famous sol-gel method was used by dispersing titanium nano-oxide in ethanol (v/v 1:3).

2.2.2. Preparation of Methyl Ammonium Lead Tri-Iodide Perovskite ($CH_3NH_3PbI_3$) Precursors

Precursor A (PbI_2): 4.6 g Lead Iodide (PbI_2) was mixed with dimethylformamide. This mixture was placed in a molten wax bath and heated at 250 ^{o}C for 45 minutes.

Precursor B (MAI): 20 ml of dried isopropanol was mixed with 0.32 g of methylammonium iodide and shaked for 3 minutes until there was no traces of any whitish residue.

2.3. Preparation of the Photoanodes

The Fluorine doped Tin Oxide (FTO) glass substrate with sheet resistance of 15 Ω square^{-1} was cleaned using sodium laureth sulphate. The compact layer (c-TiO_2) film was dynamically spin-coated on the FTO with the condition of 4000rpm for 20 seconds. It was dried at 120 ^{o}C for 10 minutes and thereafter annealed at 450 ^{o}C for 30 minutes. The m-TiO_2 was deposited using spin coating procedure at 4000rpm for 20 seconds and annealed at 500 ^{o}C for 30 minutes. For the controlled device, few drops of the prepared Precursor A was dynamically spin-coated and followed immediately by the dynamic spin-coating of precursor B both in the glove box. The formation of dark perovskite layer was observed after which it was immersed in a beaker containing propanol for 5 minutes to expel excess MAI. The resulting photoanode containing FTO/c-TiO_2/m-TiO_2/$MAPbI_3$ was then annealed for 10 minutes at 120 ^{o}C. For the second device, the synthesized GO colloid was deposited by drop casting procedure on the substrate containing c-TiO_2/m-TiO_2. The resulting substrate of FTO/c-TiO_2/m-TiO_2/GO was then treated at 120 ^{o}C for 5 minutes and then raised to 230 ^{o}C for 10 minutes to allow adequate thermal reduction of GO to reduced GO (rGO). Thereafter, few drops of the prepared PbI_2 was dynamically spin-coated and followed immediately by the dynamic spin-coating of the MAI precursor both in the glove box as done in the first device and annealed for 10 minutes at 120 ^{o}C. This gave a photoanode with the architecture FTO/c-TiO_2/m-TiO_2/rGO/$MAPbI_3$. For the third device, the procedure followed suit with the first device, thereafter followed by GO deposition with heat treatment from 120 ^{o}C to 230 ^{o}C to reduce GO to rGO. This gave a design of FTO/c-TiO_2/m-TiO_2/$MAPbI_3$/rGO. The last device has the architecture FTO/c-TiO_2/m-TiO_2/rGO/$MAPbI_3$/rGO which was prepared following the initial methods in device one, two and three.

2.4. Preparation of Counter Electrode

A composite material consisting of carbon black and graphite (CBG) in a ratio 3:1 respectively was utilized. This follows from the well-known protocol of Zhang et. al. [30]. The CBG was cut into a circular shape of area 0.786 cm^2.

2.5. Assembly of the Cells

The four PSCs were assembled by sealing the four photoanodes and the counter electrodes using Ethylene-Vinyl Acetate (EVA).

2.6. Characterization and Measurement

1. The morphology of rGO nanofilm was studied using the Scanning Electron Microscope (SEM) (Phenom ProX PW-100-012 model).
2. Raman spectroscopy (ProRaman-L-785-B1S with serial number 196166) was utilized to identify the functional groups.
3. Structural analyses of the fabricated films were performed using X-ray Diffractometer (XRD), (Rigaku D, Max 2500, Japan).
4. Optical spectra were characterized using ultraviolet–visible light (UV–vis) spectrometer (Axiom Medicals UV752 UV-vis-NIR).
5. The hall effect measurement was done using a four-point probe (ECOPIA HMS-3000 version 3.52) at room temperature (300 K).
6. The current density-voltage performance of the PSCs were estimated using a solar simulator (Newport Corporation) and a Keithley 2400 (Keithley, Inc.) source-meter. The performance characteristics of the solar cells were evaluated under 1 sun illumination (AM 1.5G standard test conditions at 100 mWcm^{-2}).

3. Results and Discussion

3.1. Scanning Electron Microscope

Figure 1 shows the SEM Images of (a) rGO with a Magnification of 2000x, (b) rGO with a Magnification of 500x, and (c) Mesoporous TiO_2 with a Magnification of 1000x. The obtained images of the rGO at different magnification revealed a crumpled surface with distinct edges and rippled structures with haphazardly aggregated islands at the surface of the rGO nanofilms which is attributed to the after effect of the exfoliation process of GO sheets from graphite. More so, it is evident from the SEM images that the rGO film is corrugated which shows the intrinsic strength nature of graphene materials. The irregularity as observed could be as a result of incomplete oxidation. However, this can serve as a good potential site for the absorbing material [31].

Figure 1(c) shows the structural morphology of the mesoporous TiO_2. The resulting image depicts a homogeneous film with the presence of nanopores which are suitable sites for the adsorption of the absorbing layer. Furthermore, it is evident from the visualized nanopores that the mesoporous layer would allow passage or tunneling of the rGO and/or the harvesting material as the case may be thereby, enhancing good ohmic contact with the compact layer and other functionalized layers. In

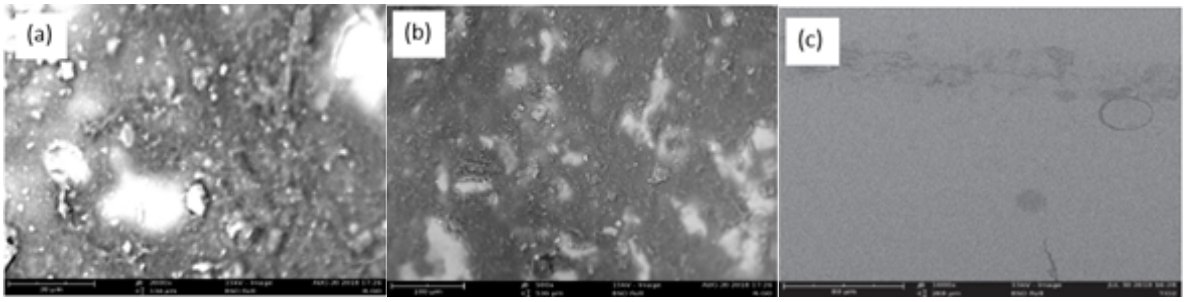

Figure 1. SEM Image of (a) rGO with a Magnification of 2000x, (b) rGO with a Magnification of 500x, and (c) Mesoporous TiO_2 with a Magnification of 1000x

addition, the nanopores will serve as growth nucleation sites for good crystallinity for the rGO and harvesting material during thermal annealing. This crystallinity which is a function of the nucleation growth has been found to have its immense role in the electronic performance of the devices. Hence, the morphological structure of both the rGO and the mesoporous TiO_2 shows good morphology as expected of any material that will be classified either as a buffer layer. The SEM image also shows some macroscopic defects which is due to transfer of samples during characterization.

3.2. Raman Spectroscopy Result Analysis

Figure 2 shows the active spectrum of Raman peaks at varying Raman bands (Raman Shift or wavelengths). By using the Lorentzian deconvolution fit on OriginLab8, sharp Raman epicenters were observed at 2076 cm^{-1} (D-band), 2080 cm^{-1} (G-band) and 2886cm^{-1} (2D-band) for the rGO.

The prominent Raman signal at 2080 cm^{-1} designated by the G-band is attributed to the strong manifestation of *sp* hybridization of carbon atoms resulting from the unsaturated triple bond of carbon atoms (C≡C) which correlates with some Raman bands [5]. The D-band at 2076 cm^{-1} is ascribed to the presence of defects in the *sp* lattice and related to defects (edge, vacancy and ripples) in the graphene structure which was as observed from our reported SEM image in this study [32]. The 2D band peak observed at 2886 cm^{-1} is credited to the oxidation of the graphene structure with the presence of oxygen and hydrogen functional group. This is as evident from the active Raman band standard table. It can be inferred from the *sp* hybridization that the rGO is conjugated which implies a high level of delocalized electrons (resulting from the π-electrons from p-orbitals) which in general lowers energy required for charge exciton and also increases stability thereby establishing the latter analysis on the absorbance study of the role of rGO in enhancing absorptivity of PSCs. Furthermore, the hydrophobic and electrophilic nature of this class of material can be attributed to the cyclo-addition from the oxygenation process resulting from the triple bond [5].

It is worthy of note that the Raman data for the rGO suffices since it's the final material used in the fabrication of the cell.

The D/G band intensity ratio (I_D/I_G) and 2D/G band intensity ratio (I_{2D}/I_G) provides valuable insights about the structure of graphene and graphene materials which help us appreciate the numbers particularly when structural analysis cannot be

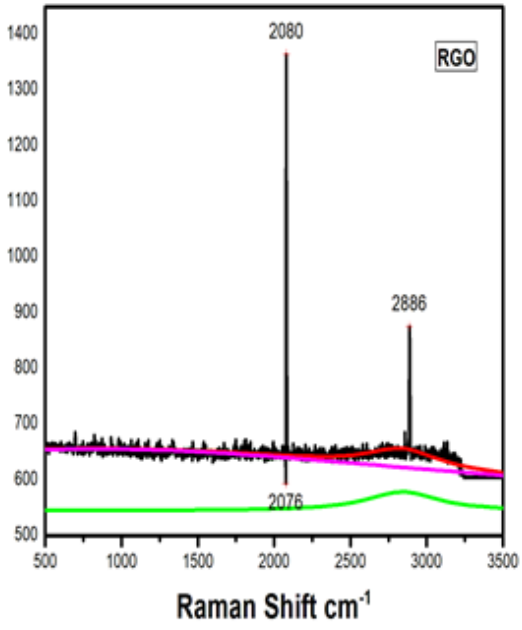

Figure 2. Deconvoluted Intensity-Wavenumber for Active Raman Peaks of rGO

achieved. The I_D/I_G represents the defect density [33, 34] while I_{2D}/I_G denotes the numbers of layers [35] present in graphene materials.

It is evident from Table 1, that the D, G and 2D bands significantly have different intensity that helps in making meaningful inference in the applicability of rGO. The I_D/I_G column implies that the rGO contains defects thereby affirming our morphological analysis. In addition, the I_{2D}/I_G band suggests that, the reduced graphene oxide as synthesized consist of multilayers of graphene with an increased number of functional groups and delocalized electrons. This further attest to our analysis on the presence of high number of delocalized electrons in our rGO film which shows prospects for photovoltaic and photonic applications. However, the increase in number of electrons and minimal defect in the rGO films makes it more applicable thereby informing our choice of which graphene material is to be incorporated in the fabrication of our solar devices.

Table 1. Peaks, intensity and intensity ratio band of synthesized films of rGO from raman spectrum

Sample	D Band	G Band	2D Band	I_D Band	I_G Band	I_{2D} Band	I_D/I_G Band	I_{2D}/I_G Band
rGO	2076.0000	2080.0000	2886.0000	593.6047	1365.0359	875.6639	0.4348	0.6415

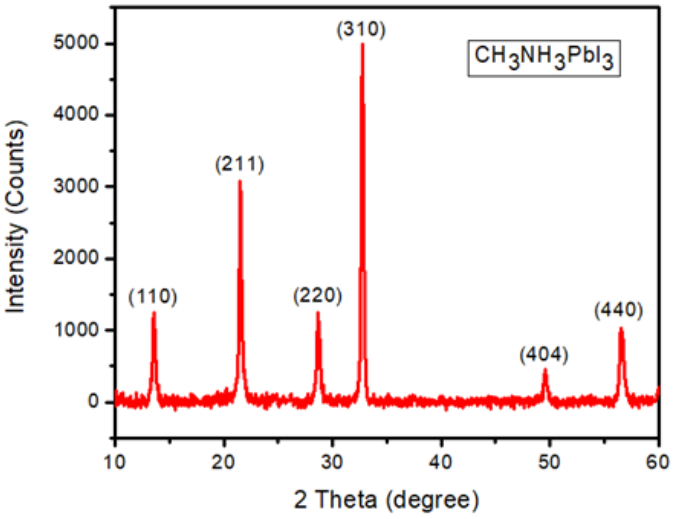

Figure 3. X-ray diffraction pattern of $CH_3NH_3PbI_3$

3.3. X-ray Diffraction

To ascertain the complete formation of the perovskite absorber ($CH_3NH_3PbI_3$) layer in this research, the XRD measurement was carried out on the synthesized methylammonium absorber thin film. As depicted from Figure 3, the main peaks at 2θ angles of 14.0°, 28.6°, 31.9° corresponding to the 110, 220 and 310 planes confirms the formation of $CH_3NH_3PbI_3$ [10, 36]. The formed $CH_3NH_3PbI_3$ film is of high crystalline quality.

3.4. UV- Vis Spectrophotometry Analysis

The absorptivity of varying configurations on FTO glasses consisting of m-TiO_2, rGO and the perovskite film were investigated using UV-750 Series spectrophotometer within the range 230-1200 nm of wavelengths. The graphical representation of each configuration as deposited on FTO glass slides for necessary investigation are presented in Figure 4. However, the absorption as reported was normalized by dividing through by the observed absorbance peak thereby resulting in an absorbance value between 0 and 1. As shown in the combined absorbance of the samples, m-TiO_2 shows a shouldering peak at 333 nm in the ultraviolet (UV) region. The undulating absorbance between 230-290 nm can be attributed to the non-bonding to the pi bonding excitations of the material [37]. At such a wavelength, no visible light will be absorbed. With m-TiO_2 being an electrode, the plot justifies that the material is not capable of harvesting light within the spectrum since no significant absorbance was observed. The rGO absorbs light partly from the UV region through the near infrared (NIR) region with observable peaks from 500-860 nm and a noticeable absorbance peaks of 516 nm and 640 nm within the visible region. The wide range of absorbance can be ascribed to the zero-band gap of graphene which is also in tandem with its broad range theoretical absorbance capacity up to the microwave region. This also informs the presence of several delocalized electrons (π-π^* bonding). As earlier stated, the undulating absorbance between 230-290 nm can be attributed to the non-bonding to the pi bonding transition while the nonlinear absorption behavior (saturation absorption) of rGO can be ascribed to the exposure of the rGO films to air and possibly the presence of Nitrogen [38]. Also, a sharp increment was observed around 995 nm which is an attestation to the ability of this class of materials to absorb adequately at this region.

Furthermore, the plot shows a more stable absorption rate over a wide-range of wavelength within the visible region from 385-538 nm for the absorbing material with a maximum absorbance peak at 386 nm. This can be attributed to the high absorption coefficient of this class of material as stated earlier. A sharp shouldering pattern was observed from 530 nm up to the NIR which could be as a function of the degradation pattern of this class of materials. Although, an eventual increment was noticed at about 1000 nm. Above all, the harvesting material demonstrated a good absorbance across the entire visible region.

Similarly, it is evident that in the presence of rGO, a hyperchromic effect by an average of 27.78% was observed at the same wavelength of 1000 nm after incorporating rGO on m-TiO_2. This depicts the possibility of rGO to absorb photons due to delocalized electrons and above all proving to be of positive effect to the photoanode.

However, the absorbance peak for the m-TiO_2/Perovskite configuration was at 386 nm. It is evident that in the presence of m-TiO_2, the absorptivity of the harvesting material witnessed no significant boost. However, a slight flattening was detected across the peaks in the plot in comparison with the perovskite absorbance graph. The implication of this according to the energy and wavelength relationship is that more energy will be required for the excitation of electrons as the gap between the HOMO and LUMO must have likely increased. Hence, this suggests a serious need for an interlayer that will bridge the energy gap between both layers which rGO proves to be suitable.

Nonetheless, it was depicted that the underlayer introduction of the perovskite material with rGO resulted in a bathochromic effect (red shift). The implication of this is that in the presence of the rGO, there is an increase in the number of delocalized electrons of the absorbing material thereby leading to a quasi-fermi level as there's likely to have been a fall in the gap between the HOMO and LUMO. Similarly, lesser energy will be required in exciting electrons as the work function must have been lessened. A close look at the UV region indicates a

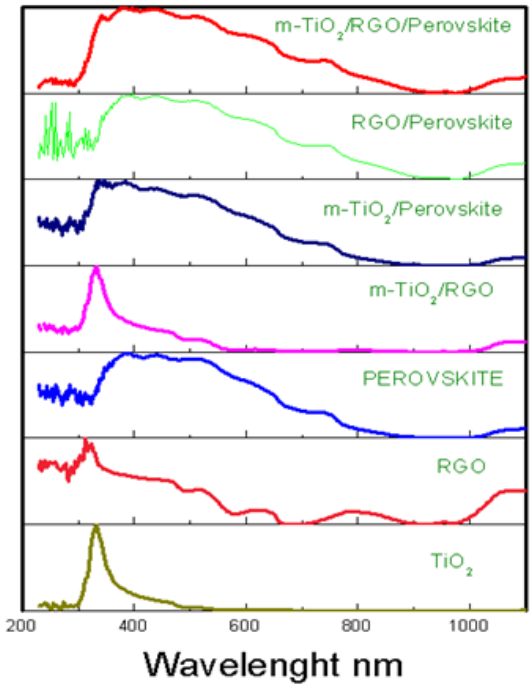

Figure 4. A stacked graph Showing the Absorbance spectrum of all Sample Configurations at a Glance

hyperchromic effect across the UV region with a significant rise in the minimum absorbance. In addition, adequate broadening of peaks was witnessed across the visible region. Summing up all, this configuration shows that the rGO is a very good material with promising outputs for photovoltaic applications in Perovskite Solar Cells.

Also, the figure also shows the absorptivity for the configuration with rGO as an interlayer between the m-TiO_2 and the absorbing material. It is evident that the effect of the rGO has helped in addressing the "no effect" as observed in the m-TiO_2/Perovskite architecture by enhancing an absorbance peak of 433 nm within the absorbing range of 350-535 nm with a protruding peak at 958 nm as well as a stable shouldering. The observed red shift would likely be as a result of increased delocalization of electron taking place by using rGO as an interlayer material. More so, the rise in HOMO and LUMO inferred in the m-TiO_2/Perovskite can as well be inferred to have fallen with an upper bound hypochromic effect and lower bound hyperchromic effect in absorptivity. What this implies is the formation of a quasi-fermi level which lessens the work function of this architecture. Hence, devices with rGO as an interlayer between the mesoporous transport layer and the harvesting material in this architectural configuration will be energetically favored since lesser energy will be required for the excitation of excitons. Since more work will be done with less energy, this translates to devices with this configuration having a better efficiency.

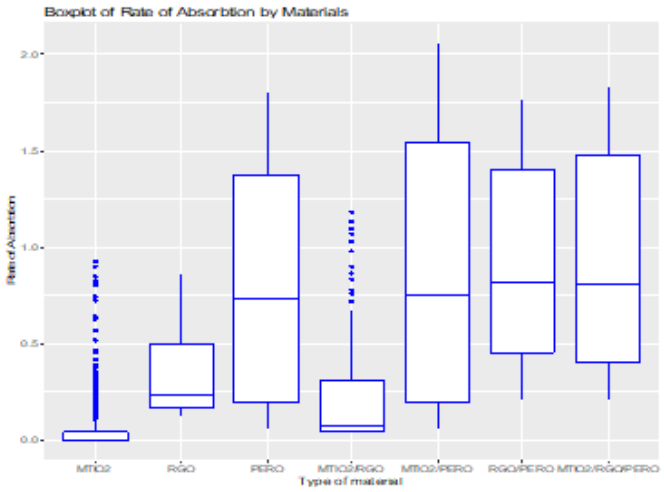

Figure 5. Box Plot Describing the Absorbance Behavior of each Sample Configuration

3.5. *Statistical Analysis of UV-Vis Spectrophotometry*

Data analysis may be rendered incomplete without some statistical analysis that helps us verify our scientific inferences by using applicable statistical models. Herein, statistical Analysis of Variance (ANOVA) was carried out to know the significant difference in the mean rate of absorptivity of the demonstrated samples. Although the set of data under consideration are skewed, affected by outliers and not normally distributed thereby requiring a non-parametric test. However, with a data frequency of 314, the outliers are believed to likely not have any significant effect on the result thus the justification for the use of ANOVA. Also, a Post Hoc comparison using Duncan multiple range test (DMRT) was used to show specifically the variation in each sample. The Duncan multiple range test as proposed by Duncan is a statistical analysis tool that gives results by comparing the specific difference in the means of various data set and in our case gives result on the difference between the mean absorbance of various sample configurations. In addition, a box plot was used to show the maximum, minimum and median absorbance. With a box plot, a more crystal role of the effect of the rGO on absorbance pattern of the configuration can be deduced. The descriptive statistics in Table 2 gives an overview of the entire data set. It is worthy of note to state that the statistical analysis which includes the box plot and the descriptive analysis was carried out using a statistical programing software called R.

The descriptive analysis shows that the number of data set for each configuration is 314. This implies that the samples were bombarded with 314 different monochromatic light between the wavelength of 200-1200 nm. It also gives the overall mean absorbance to fall within (0.06542-0.90976) with rGO/Perovskite having the highest mean rate of absorption. Also, the standard deviation and error associated to each configuration, the upper and lower class bound as well as the minimum and maximum value for each sample were included.

1. **Descriptive Statistics**

Table 2. Statistical Description of the Absorbance Behavior of all Configurations

Rate of absorption					95% CI		Min	Max
Type of Materials	N	Mean	Std. Deviation	Std. Error	Lower Bound	Upper Bound		
m-TIO_2	314.0	0.06542	0.15342	0.00866	0.04838	0.08245	0.00002	0.92500
rGO	314.0	0.32990	0.18625	0.01051	0.30922	0.35058	0.12000	0.85700
Perovskite	314.0	0.79691	0.61023	0.03444	0.72916	0.86467	0.06200	1.80000
m-TIO_2/rGO	314.0	0.19063	0.21810	0.01231	0.16642	0.21485	0.03700	1.18200
m-TIO_2/Perovskite	314.0	0.86232	0.67983	0.03837	0.78684	0.93781	0.06300	2.06100
rGO/Perovskite	314.0	0.90976	0.51627	0.02913	0.85244	0.96709	0.20900	1.76300
m-TIO_2/rGO/Perovskite	314.0	0.89379	0.55844	0.03151	0.83178	0.95580	0.20900	1.83100

The box plot in Figure 5 depicts the distribution of the rate of absorption disaggregated by the type of materials. It's evident that doping of m-TIO_2 with rGO (m-TiO_2/rGO) resulted in a significant increment in both the minimum and maximum values of m-TiO_2 which is in accordance with the observed hyperchromic effect. Similarly, the box plot revealed the role of rGO as an underlayer material for perovskite material with a significant enhancement in the minimum absorption and slight increment in maximum absorption. This agrees with the red shift as earlier analyzed. While the m-TiO_2/Perovskite material shows the highest absorption as a result of the blue shift, the m-TiO_2/rGO/Perovskite also indicate a significant increment in the minimum absorbance and a slight drop in the maximum absorbance. Therefore, showing the role of rGO as an efficient interlayer between the m-TiO_2 and absorbing material.

2. **Analysis of Variance (ANOVA) Result**

Hypothesis:

The analysis of variance carried out is based on the following two hypotheses:

H_o: There is no significant difference in the rate of absorption across the materials

H_1: There is a significant difference in the rate of absorption across the materials

Table 3 depicts the result of One-way between groups analysis of variance conducted at a 99 % confidence interval to explore the impact of materials on the rate of absorption. The mean rate of absorption by combining different materials were compared and the result which conforms with previous comparative analysis shows that there was a statistically significant difference between the rate of absorption across the various types of materials, with F (6, 2191) = 196.078, and a probability value (p-value= <0.001) which is < 0.01. Hence, by convention, we discard our null hypothesis (H_o) and uphold the research hypothesis that says that there is a significant difference between the sample configurations. Although, the post hoc comparison using Duncan Multiple Range Test will help us to know which is significantly different from the other.

3. **Duncan Multiple Range Test**

Duncan multiple range test (Table 4) reveals no significant difference between rGO/Perovskite and m-TiO_2/rGO/Perovskite as well as m-TiO_2/Perovskite and Perovskite. However, the same result shows that a significant difference exists between: rGO/Perovskite and Perovskite; m-TiO_2/rGO and rGO. Furthermore, it depicts that rGO/Perovskite is significantly different from m-TiO_2/Perovskite. Similarly, the combinations of each of m-TiO_2/Perovskite, rGO/Perovskite and m-TiO_2/rGO/Perovskite is significantly different from the individual usage of each of rGO, m-TiO_2 and Perovskite. Hence, the significance of rGO as inferred earlier is further justified both statistically.

3.6. Hall Effect Result and Analysis

Table 5 depicts that the nature of charge carriers in this material are electrons which is evident from the negative sign (-) in the bulk and sheet concentration value. The concentration of the delocalized electrons affirms our observations from the Raman results and also conforms with the inference from our absorbance analysis thereby making the material suitable for solar device application. Similarly, the material shows a very good electron mobility, conductivity and resistance

3.7. Photovoltaic Performance of the PSCs

In obtaining the electrical properties of the fabricated cells, Device A-D were simulated using the A. M. 1.5G Solar simulator. From the obtained results (J_{SC} and V_{OC}) as measured, the Fill Factor (FF), Power Conversion Efficiency (PCE), were obtained from Equations 1 and 2 as reported in Table 6.

$$FF = \frac{J_{\max} \times V_{\max}}{J_{SC} \times V_{OC}} \tag{1}$$

$$PCE = \frac{FF \times J_{SC} \times V_{OC}}{P_{IRRADIANCE}}.100\% \tag{2}$$

where FF is Fill Factor, PCE is solar cell efficiency, V_{max} is maximum voltage, J_{max} is maximum current density, J_{sc} is short circuit current density, V_{oc} is open circuit voltage and $P_{IRRADIANCE}$ is light intensity.

From Table 6, it was observed that the insertion of rGO has no significant effect on the short circuit current density Jsc as the devices exhibit relative Jsc value of $8.007 \leq Jsc \leq 8.737$. This relativity is indicative of the optical trapping capability of all the devices for photovoltaic conversion. Although, there is a slight drop in the Jsc value for device B which could have been due to the thickness of the rGO film thereby limiting optical

Table 3. One-Way ANOVA Result for the Absorptivity of tested samples

Source of variation	Sum of Squares	df	Mean Square	F	p-value
Between Groups	255.249	6	42.541	196.078	<0.0001
Within Groups	475.363	2191	0.217		
Total	730.612	2197			

Note that the null hypothesis is to be discarded if p-value is less than 0.01.

Table 4. Duncan Multiple Range Test Result for the Absorptivity of tested samples

Duncan						
		Subset for alpha = 0.05				
Type of material	N	1	2	3	4	5
m-TIO_2	314	.0654172				
m-TIO_2/rGO	314		.1906338			
rGO	314			.3299045		
PEROVSKITE	314				.7969140	
m-TIO_2/PEROVSKITE	314				.8623217	.8623217
m-TIO_2/rGO/PEROVSKITE	314					.8937898
rGO/PEROVSKITE	314					.9097611
Sig.		1.000	1.000	1.000	.079	.231

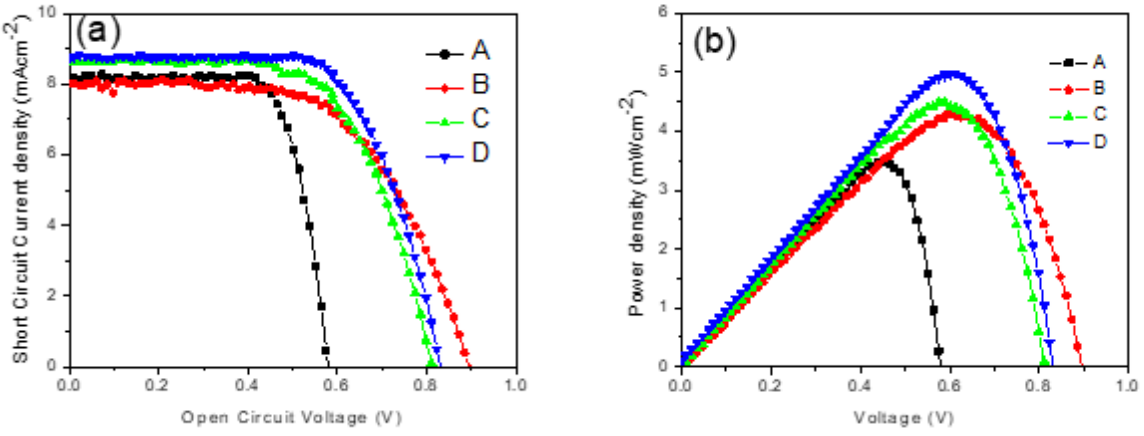

Figure 6. Comparative Graph of current against voltage for Devices A, B, C and D

Table 5. Parametric Results from the Hall Effect Measurement System

Parameters	Result
Bulk Concentration	$-9.878\times10^{13}/cm^3$
Mobility	2.099×10^4 cm^3/Vs
Sheet Resistance	1.434×10^5 ?/cm^2
Resistivity	3.011 ?cm
Sheet Concentration	$-2.074\times10^9/cm^2$
Conductivity	3.321×10^{-1}

transmittance of the device. Above all, the Jsc result suggests good ohmic contact amongst the layers of the fabricated devices.

However, it is evident that a significant boost was witnessed in the open circuit voltage of devices with rGO interlayer. A minimum of 23.21 % increment in PCE was observed between the control device without rGO and other devices with rGO. While the Voc value ranges within $0.575 \leq V_{oc} \leq 0.886$, the enhancement can be attributed to the ability of the rGO to minimize interfacial recombination from both charge transport interface with the absorbing layer. The recombination suppression is due to the rough adhesive surface of the rGO film as depicted by the SEM image. Furthermore, the Voc heightening can be credited to the ferroelectric distortion of the perovskite when in contact with graphene materials. The distortion is capable of improving charge carrier extraction along the interfaces, regeneration of the active layer through enhanced charge transfer from the perovskite absorbing layer to the electron/hole transport layers. This submission is supported by the theoretical demonstration of Volonakis and Guistino [39]. In their work, they ascertained that the ferroelectric distortion leads to tilt in the crystallinity of the perovskite material thereby causing a

Table 6. Photovoltaic Performance Parameters of devices A, B, C and D

Device	Architecture	Jsc(mA/cm^2)	Voc (V)	FF (%)	PCE (%)
A	glass/FTO/c-TiO_2/m-TiO_2/$MAPbI_3$/CBG	8.151	0.575	74.4	3.49
B	glass/FTO/c-TiO_2/m-TiO_2/rGO/$MAPbI_3$/CBG	8.007	0.886	60.6	4.30
C	glass/FTO/c-TiO_2/m-TiO_2/$MAPbI_3$/rGO/CBG	8.659	0.811	64.0	4.49
D	glass/FTO/c-TiO_2/m-TiO_2/rGO/$MAPbI_3$/rGO/CBG	8.737	0.836	68.1	4.98

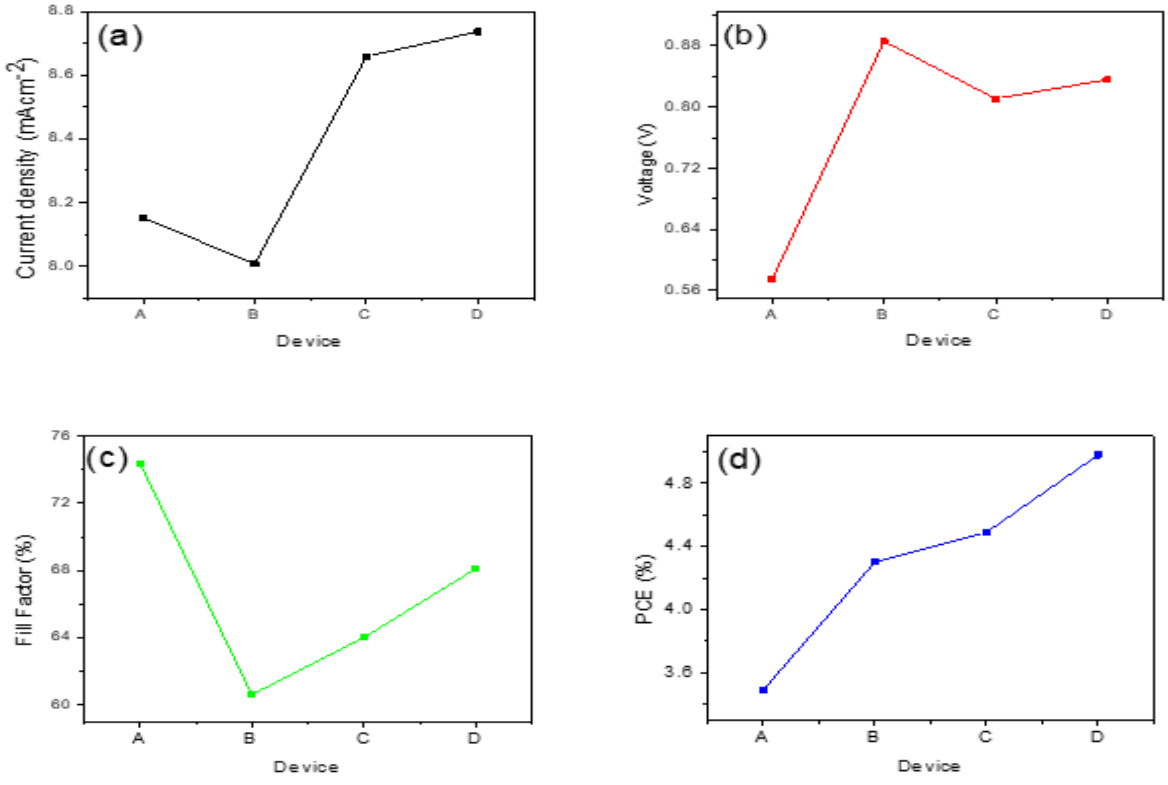

Figure 7. Variation of (a) Jsc, (b) Voc, (c) FF and (d) PCE with device having various Photoanode

change in the electronic and structural properties of the perovskite.

In furtherance, the device D which comprises of the synergistic architecture harnessed the properties of rGO at both the electron and hole interface in: trapping and converting photon energy, minimizing recombination, enhancing hole and electron extraction -cum tunneling and the regeneration of the harvesting material all of which resulted in its heightened PV value and enhanced conversion efficiency as observed. The observed Jsc, Voc, and FF values for the reference device were 8.151 mA cm^{-2}, 0.575 V, and 74.4 %, respectively, yielding a PCE of 3.49 %. The best PCE in our research, was achieved using rGO incorporated on both TiO_2 and $MAPbI_3$. Particularly, the device showed a Jsc of 8.737 mA cm^{-2}, Voc of 0.836 V, and FF of 68.1 %, respectively, resulting to a PCE of 4.98 % (see Figure 6a). The highest device was ~ 42.69 % higher than that of the reference device, suggesting that the addition of rGO can improve the PCE of PSCs. This improvement in the power conversion efficiency may be attributed to the higher electrical conductivity and suitable energy band alignment of our rGO in the device [2].

Figure 6b shows the relationship that exist between the power density and open circuit voltage. Figure 7 (a-d), show the metric parameters dependence with various photoanode. The optimum performance was with device having rGO on both ETL and HTM.

4. Conclusion

The effect of Reduced Graphene Oxide on the performance metrics (PCE, Jsc, Voc, and FF) of perovskite solar cells was investigated systematically. As a result, the device performance such as Jsc and PCE were enhanced with rGO introduction as compared to the pure device without rGO. The champion device was achieved with the architecture of FTO/c-TiO_2/m-TiO_2/rGO/$CH_3NH_3PbI_3$/rGO/CBG resulting to improvement from 8.151 to 8.737 $mAcm^{-2}$ in Jsc and from 3.49

to 4.98 % in PCE respectively. The obtained results show an enhancement of ~42.69 % in PCE and ~ 7.20 % in Jsc over the prestine device. These results were encouraging and demonstrated good means of enhancing perovskite solar cell performance using reduced graphene oxide.

Acknowledgments

The authors are grateful to Physics Advanced Laboratory, Sheda Science Technology Complex (SHESTCO) and Namiroch research Laboratory, Abuja for the use of their equipment.

References

[1] Z. Qu, F. Ma, Y. Zhao, X. Chu, S. Yu & J. You, "Updated progresses in perovskite solar cells", Chinese Physics Letters **38** (2021) 107801.

[2] S. Suragtkhuu, O. Tserendavag, U. Vandandoo, A. S. R. Bati, M. Bat-Erdene, J. G. Shapter, M. Batmunkh & S. Davaasambuu, "Efficiency and stability enhancement of perovskite solar cells using reduced graphene oxide derived from earth-abundant natural graphite", RSC Advances **10** (2020) 9133.

[3] J. Duan, H. Xu, W. E. I. Sha, Y. Zhao, Y. Wang, X. Yang & Q. Tang, "Inorganic perovskite solar cells: an emerging member of the photovoltaic community", Journal of Materials Chemistry A **7** (2019) 21036

[4] H. Wang, X. Liang, J. Wang, S. Jiao & D. Xue, "Multifunctional inorganic nanomaterials for energy applications", Nanoscale **12** (2020) 14.

[5] Q. Guo, F. Yuan, B. Zhang, S. Zhou, J. Zhang, Y. Bai, L. Fan, T. Hayat, A. Alsaedi & Z. Tan, "Passivation of the grain boundaries of $CH_3NH_3PbI_3$ using carbon quantum dots for highly efficient perovskite solar cells with excellent environmental stability", Nanoscale **19** (2019) 115.

[6] M. Batmunkh, K. Vimalanathan, C. Wu, A. S. R. Bati, L. Yu, S. A. Tawfik, M. J. Ford, T. J. Macdonald, C. L. Raston, S. Priya, C. T. Gibson & J. G. Shapter, "Efficient production of phosphorene nanosheets via shear stress mediated exfoliation for low-temperature perovskite solar cells", Small Methods **3** (2019) 1800521.

[7] J. D. Chen, T. Y. Jin, Y. Q. Li & J. X. Tang, "Recent progress of light manipulation strategies in organic and perovskite solar cells", Nanoscale **11** (2019) 18517.

[8] G. Mathiazhagan, L. Wagner, S. Bogati, K. Y. Unal, D. Bogachuk, T. Kroyer, S. Mastroianni, & A. Hinsch, "Double-mesoscopic hole-transport-material-free Perovskite solar cells: overcoming charge-transport limitation by sputtered ultrathin Al_2O_3 isolating layer", ACS Applied Nano Materials **3** (2020) 2463.

[9] L. Wagner, S. Chacko, G. Mathiazhagan, S. Mastroianni & A. Hinsch, "High photovoltage of 1 V on a steady-state certified hole transport layer-free Perovskite solar cell by a molten-salt approach", ACS Energy Letters **3** (2018) 1122.

[10] E. Danladi, M. Y. Onimisi, S. Garba & J. Tasiu, "9.05 % HTM free perovskite solar cell with negligible hysteresis by introducing silver nanoparticles encapsulated with P_4VP Polymer", SN Applied Sciences **2** (2020) 1769.

[11] M. Saliba, T. Matsui, K. Domanski, J. Y. Seo, A. Ummadisingu, S. M. Zakeeruddin, J. P. Correa-Baena, W. R. Tress, A. Abate, A. Hagfeldt & M. Gratzel, "Incorporation of rubidium cations into " perovskite solar cells improve photovoltaic performance", Science **354** (2016) 206.

[12] G. Grancini, C. Roldan-Carmona, I. Zimmermann, E. Mosconi, X. Lee, D. Martineau, S. Narbey, F. Oswald, F. D. Angelis, M. Graetzel & M. K. Nazeeruddin, "One-Year stable perovskite solar cells by 2D/3D interface engineering", Nature Communications **8** (2017) 15684.

[13] X. Li, M. Tschumi, H. Han, S. S. Babkair, R. A. Alzubaydi, A. A. Ansari, S. Habib, M. K. Nazeeruddin, S. M. Zakeeruddin & M. Gratzel, "Outdoor performance and stability under eelevated temperatures and long-term light soaking of triple-layer mesoporous perovskite photovoltaics", Energy Technology **3** (2015) 551.

[14] T. Y. Yang, N. J. Jeon, H. W. Shin, S. S. Shin, Y. Y. Kim & J. Seo, "Achieving long-term operational stability of perovskite solar cells with a stabilized efficiency exceeding 20% after 1000 h", Advanced Science 6 (2019) 1900528.

[15] J. Chen, X. Cai, D. Yanga, D. Song, J. Wang, J. Jiang, A. Ma, S. Lv, M. Z. Hu & C. Ni, "Recent progress in stabilizing hybrid Perovskites for solar cell applications", Journal of Power Sources **355** (2017) 98.

[16] C. Zhi, Z. Li & B. Wei, "Recent progress in stabilizing perovskite solar cells through two-dimensional modification", APL Materials **9** (2021) 070702.

[17] H. Choi, K. Choi, Y. Choi, T. Kim, S. Lim & T. Park, "A review on reducing grain boundaries and morphological improvement of perovskite solar cells from methodology and material-based perspectives, small methods", Small methods (Special Section: Perovskite Solar Cells) **4** (2020) 1900569.

[18] D. Kim, K. Higgins & M. Ahmadi, "Navigating grain boundaries in perovskite solar cells", Matter **4** (2021) 1442.

[19] M. Que, B. Zhang, J. Chen, X. Yin & S. Yun, "Carbon-based electrodes for perovskite solar cells", Materials Advances **2** (2021) 5560.

[20] D. Bogachuk, B. Yang, J. Suo, D. Martineau, A. Verma, S. Narbey, M. Anaya, K. Frohna, T. Doherty, D. Müller, J. P. Herterich, S. Zouhair, A. Hagfeldt, S. D. Stranks, U. Würfel, A. Hinsch & L. Wagner, "Perovskite solar cells with carbon-based electrodes – quantification of losses and strategies to overcome them", Advanced Energy Materials **12** (2022) 2103128.

[21] M. Hadadian J. H. Smått & J. P. Correa-Baena, "The role of carbon-based materials in enhancing the stability of perovskite solar cells", Energy and Environmental Science **13** (2020) 1377.

[22] K. Moore & W. Wei, "Applications of carbon nanomaterials in perovskite solar cells for solar energy conversion", Nano Materials Science **13** (2021) 276.

[23] E. Nouri Y. L. Wang Q. Chen J. J. Xu G. Paterakis, V. Dracopoulos, Z. X. Xu, D. Tasis, M. R. Mohammadi & P. Lianos, "Introduction of graphene oxide as buffer layer in perovskite solar cells and the promotion of soluble n-Butyl-substituted copper phthalocyanine as efficient hole transporting material", Electrochimica Acta **233** (2017) 36.

[24] E. Nouri, M. R. Mohammadi, Z. X. Xu, V. Dracopoulos & P. Lianos, "Improvement of the photovoltaic parameters of perovskite solar cells using a reduced-graphene-oxide-modified titania layer and soluble copper phthalocyanine as a hole transporter", Physical Chemistry Chemical Physics **20** (2018) 2388.

[25] K. Gong, J. Hu, N. Cui, Y. Xue, L. Li, L. Long & S. Lin, "The roles of graphene and its derivatives in perovskite solar cells: A review", Materials & Design **211** (2021) 110170.

[26] E. Kusrini, I. Ramadhani, M. I. Alhamid, N. Y. Voo & A. Usman, "Synthesis and adsorption performance of graphene oxide-polyurethane sponge for oil-water separation", Engineering Journal **26** (2022) 1.

[27] G. Santamaría-Juárez, E. Gómez-Barojas, E. Quiroga-González, E. Sánchez-Mora, M. Quintana-Ruiz & J. D. Santamaría-Juárez, "Safer modified Hummers' method for the synthesis of graphene oxide with high quality and high yield", Materials Research Express **6** (2020) 125631.

[28] W. S. Hummers & R. E. Offeman, "Preparation of graphitic oxide", Journal of the American chemical society **80** (1958) 1339.

[29] K. Wojciechowski, M. Saliba, T. Leijtens, A. Abate & H. J. Snaith, "sub-150 C processed meso-superstructured perovskite solar cells with enhanced efficiency", Energy Environment Science **7** (2014) 1142.

[30] L. Zhang, T. Liu, L. Liu, M. Hu, Y. Yang, A. Mei & H. Han, "The effect of carbon counter electrodes on fully printable mesoscopic perovskite solar cells", Journal of Materials Chemistry A **3** (2015) 9165.

[31] K. Bansal, J. Singh & A. S. Dhaliwal, "Synthesis and characterization of graphene oxide and its reduction with different reducing agents", IOP Conference Series: Materials Science and Engineering **1225** (2022) 012050.

[32] K. Tsirka, A. Katsiki, N. Chalmpes, D. Gournis & A. S. Paipetis, "Mapping of graphene oxide and single layer graphene flakes-defects annealing and healing", Frontiers in Materials **5** (2018) 37.

[33] V. Scardaci & G. Compagnini, "Raman spectroscopy investigation of graphene oxide reduction by laser scribing", Journal of Carbon Research **7** (2021) 48.

[34] A. Ferrari & J. Robertson, "Interpretation of raman spectra of disordered and amorphous carbon", Physical Review B **61** (2000) 14095.

[35] Y. Shen & A. C. Lua, "A facile method for the large-scale continuous synthesis of graphene sheets using a novel catalyst", Scientific Reports **3** (2013) 1.

[36] P. Basumatary & P. Agarwal, "Photocurrent transient measurements in

MAPbI3 thin films", Journal of Materials Science: Materials in Electronics **31** (2020) 10047.

[37] E. Danladi, M. Y. Onimisi, S. Garba, P. M. Gyuk, T. Jamila & H. P. Boduku, "Improved power conversion efficiency in perovskite solar cell using Silver nanoparticles modified photoanode", IOP Conference Series: Material Science and Engineering **805** (2020) 012005.

[38] G. Wang, J. Yang, J. Park, X. Gou, B. Wang, H. Liu & J. Yao, "Facile synthesis and characterization of graphene nanosheets", Journal of Physical Chemistry C **112** (2008) 8192.

[39] G. Volonakis & F. Giustino, "Ferroelectric graphene-perovskite interfaces", Journal of Physical Chemistry Letters **6** (2015) 2496.